NUMERICAL STUDY OF FLOW STRUCTURES WITHIN DIFFERENT CAVITIES USING LARGE EDDY SIMULATION

Rahim Hassanzadeh[1*], Nehir Tokgoz[2], Besir Sahin[3]

[1]Department of Mechanical Engineering, Urmia University of Technology, Urmia, Iran
2Department of Energy Systems Engineering, Osmaniye Korkut Ata University, Osmaniye, Turkey
[3]Faculty of Engineering and Architecture, Mechanical Engineering Department, Cukurova University, Adana, Turkey

r.hassanzadeh@uut.ac.ir, nehirtokgoz@osmaniye.edu.tr, bsahin@cu.edu.tr

ABSTRACT: Large eddy simulation using a classic Smagorinsky sub-grid scale is applied for predicting the vortical flow structures within cavities. Here, flow within three different cavities such as rectangular, semi-circular, and triangular shapes are studied in order to examine the shape effects on the flow behavior. The ratio of cavity length per cavity depth is L/D=2.0 for all cavity shapes. On the other hand, simulations are carried out at three different Reynolds numbers such as 10^3, 10^4, and 10^5 in order to understand the effects of Reynolds number on the wake structures within cavities. It is found that flow structures change as a function of Reynolds number and geometry of cavities. In addition, numerical predictions revealed that the rectangular cavity imposes a higher drag to fluid flow at $Re=10^3$ and 10^4 in comparison to semi-circular and triangular cavities. A pressure jump or kinetic energy reduction is realized for semi-circular cavity at $Re=10^5$. The present numerical results are in good agreement with previous data available in the literature.

Keywords: Cavity, Finite Volume Method, Large Eddy Simulation, Turbulence
*Corresponding author. Tel: +98-4433980233, E-mail: r.hassanzadeh@uut.ac.ir

INTRODUCTION

Flow within cavities is seen in a wide variety of engineering applications such as nuclear and combustion, energy and hydraulic systems, aerospace applications and many other industrial applications. On the other hand, cavities are the fundamental structures and are ideal for understanding of three-dimensional flows. In the past decade, several investigations were performed on the flow within cavities. In general, previous investigations were carried out, more, on two different categories such as lid-driven cavities [1-13] and thermally driven cavities [14-17], generally. In other words, the investigation of flow structures within different cavities without lid or thermal drives have a limited data in the open literature. For example, Ozalp et al.

[18] studied the flow behavior past cavities with rectangular, semi-circular, and triangular shapes, experimentally using particle image velocimetry for the cavity length to the cavity depth ratio of L/D=2. They stated that rectangular and triangular cavities have larger amplitudes of velocity fluctuations while semi-circular cavity has the smallest amplitudes in velocity fluctuations.

Some of previous conducted numerical research studies focused on the numerical approaches using different turbulence methods. For example, Saqr et al. [19] applied a modified k-ε turbulence method for prediction of shear-driven vortex flow in a cylindrical cavity. They stated that the results of the computations demonstrated good agreements with an experimental result. Saqr et al. [20] also conducted numerical work using Large Eddy simulation (LES) with similar flow geometry and they revealed that the flow in the vortex core was laminar, although in other regions (such as the separation region) it was fully turbulent flow. Ryu and Baik [21] used RNG k-ε for study on the flow and dispersion in an urban cubic cavity. It was stated that a primary and secondary vortices including end-wall vortices appear in the cavity. On the other hand, Zhang et al. [22] applied Lattice Boltzmann method for simulation of lid-driven flow in trapezoidal cavities for Reynolds number in the range of $100 \leq Re \leq 15{,}000$. Peng and Davidson [23] applied LES method for the simulation of turbulent buoyant flow in a confined cavity. Arumuga Perumal and Dass [24] implemented the Lattice Boltzmann method for flow simulation in the two-dimensional cavity. Chen et al. [25] used a LES-based Lattice Boltzmann model to the study of turbulent double-diffusive natural convection in a square cavity. Lawson and Barakos [26] presented a review on the numerical simulations for high-speed turbulent cavity flows. Salinas-Vazquez et al. [27] applied LES for a confined square cavity flow with natural convection based on compressible flow equations. Effects of wall model and mesh study on the partial cavities were performed by Goncalves and Decaix [28].

Examination of the previous works on the cavity flow indicates that the flow field within the cavities as a function of the cavity shape and the Reynolds number was not studied in details. In addition, the study of the flow field of cavity with infinite length in spanwise direction is unique in this investigation since the previous works are almost dealt with the lid-driven cavities with finite dimensions. On the other hand, application of LES in such flows is very limited since many different recent works [29-31] were performed using LES with different subgrid scale models. For this reason, this work aims to present the vortical flow structure within three different cavity shapes such as rectangular, semi-circular, and triangular cavities at various Reynolds numbers in the range of $10^3 \leq Re \leq 10^5$ using LES. It should be mentioned that examination of LES abilities in this study is a minor purpose, but the main goal of this work is to compute and present flow structures within the cavities as a function of the cavity shape and the Reynolds number. However, implementation of LES requires some additional considerations such as higher grid resolutions and CPU power. Our results show good agreements with previous numerical predictions and experimental results.

COMPUTATION DETAILS

Flow domain and boundary conditions

In the present study, a 3-D Newtonian fluid flow within three different cavities such as rectangular, semi-circular, and triangular shapes are simulated at three various Reynolds numbers such as 10^3, 10^4, and 10^5 with respect to cavity depth, D, and free-stream velocity, U_∞. The ratio of cavity length, L, per cavity depth, D, is identical for all shapes and is equal to 2.0. The flow domain with dimensions of the 20D in the streamwise direction ($0 \leq x \leq 20D$), 5D in vertical direction ($-D \leq y \leq 4D$), and 4D in spanwise direction ($-2D \leq z \leq -2D$) is defined for all cavity cases as illustrated in Figure 1. For inlet section, lower surface, and cavity walls the Dirichlet boundary conditions are applied while at the upper surface and outlet section of flow domain the Neumann boundary conditions are used. A uniform velocity is defined for incoming flow. It should be mentioned that in order to consider the infinite cavity length in spanwise direction, the Neumann boundary conditions are implemented for side walls. A multi-block grid system is constructed for each flow domain as indicated in Figure 2. For this reason, each flow domain divided into different blocks and after that, the non-uniform grids are defined for each block in which grids with higher resolutions are applied within cavities. The numbers of control volumes are 831,000, 716,000, and 818,000 for flow domains corresponding to rectangular, semi-circular, and triangular cavity cases, respectively in which the minimum grid size is 0.02D for all cases. The grids are stretched near the wall in both streamwise and vertical directions using 8-10 nodes clustered within $y^+ \leq 10$. However, a uniform grid distribution is used in the streamwise direction. In fact, the constructed grid sizes provide a good compromise between accuracy and CPU time.

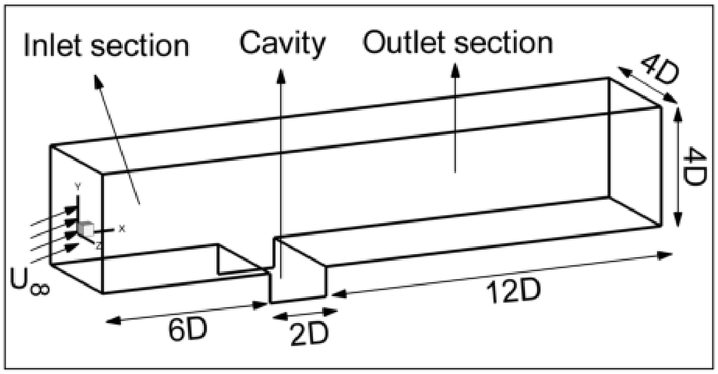

Figure 2. Schematic view of cavity, flow domain, and coordinates

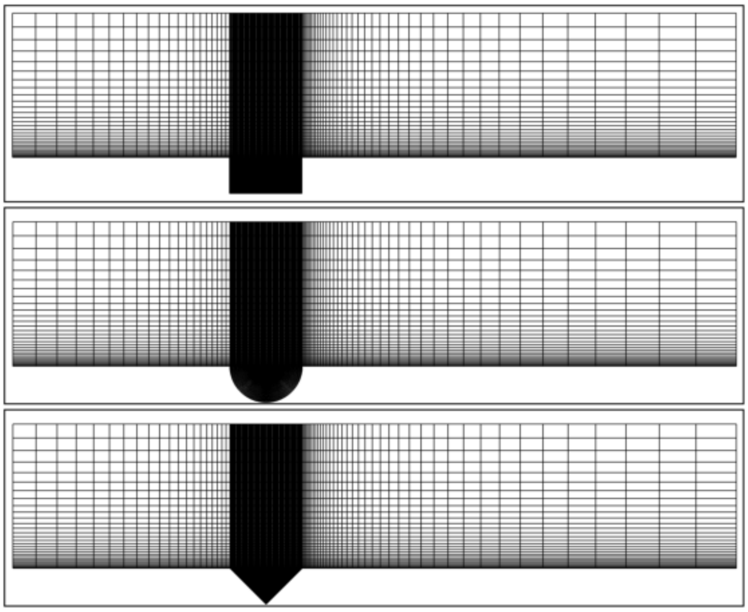

Figure 3. Multi-block non-uniform grid system

Governing equations and numerical procedure

The three-dimensional, Newtonian, and incompressible fluid flow can be modeled by

Continuity and momentum equations;

$$\frac{\partial u_i}{\partial x_i} = 0 \tag{1}$$

$$\rho \frac{\partial u_i}{\partial t} + \rho \frac{\partial}{\partial x_j}(u_j u_i) = -\frac{\partial p}{\partial x_i} + \mu \frac{\partial^2 u_i}{\partial x_j \partial x_i} \tag{2}$$

where u, ρ, p and τ are velocity, density, pressure and shear stress tensor, respectively. Here, for the simulation of vortical flow characteristics, LES is implemented and combined with Navier-Stokes equations. In LES, despite of RANS models, the small scale eddies are separated from the large scale eddies. After separation, while large scale eddies are resolved explicitly the small scale eddies are modeled like as RANS method by application of sub-grid scale (sgs) model. Separation between small scale eddies and large scale eddies become possible by introducing of a filter function. The filtering procedure is summarized as follows

$$\overline{f}(x) = \int_{-\infty}^{+\infty} f(x')G(x,x')dx' \, , \, f'(x) = f(x) - \bar{f}(x) \tag{3}$$

In equation (3), $\bar{f}(x)$, $f(x')$, and $f'(x)$ are filtered component, unfiltered function, and sgs fluctuating part, respectively. Here, G(x, x') is the filter function and has the following property

$$\int_{-\infty}^{\infty} G(x,x') = 1$$

(4)

Since there are different filtering functions for separating of eddies, in this study one of the simplest functions, which is box filter, is used. In this filtering scheme, the filter function, G(x, x'), is defined by means of local control volume size as follow:

$$G(x,x')=\begin{cases}1/\Delta & if\left|x-x'\right|\le\overline{\Delta}/2\\ 0 & otherwise\end{cases} \tag{5}$$

Here, Δ is the filter width, which is related to the local grid size by following equation:

$$\Delta=\left(\Delta V_{IJK}\right)^{1/3} \tag{6}$$

where ΔV_{IJK} is the local control volume size. After application of the filtering process, the governing equations (1) and (2) can be written as;

$$\frac{\partial\overline{u}_i}{\partial x_i}=0 \tag{7}$$

$$\frac{\partial\overline{u}_i}{\partial t}+\frac{\partial}{\partial x_j}\left(\overline{u}_i\overline{u}_j\right)=-\frac{1}{\rho}\frac{\partial\overline{p}}{\partial x_i}+\nu\frac{\partial^2\overline{u}_i}{\partial x_j\partial x_j}-\frac{\partial\tau_{ij}}{\partial x_j} \tag{8}$$

where the over-bared quantities are the filtered variables and τ_{ij} is the sgs stress tensor defined as;

$$\tau_{ij}=\overline{u_iu_j}-\overline{u}_i\overline{u}_j \tag{9}$$

There are some different sgs models, for instance, one of the old, simple, and more applicable ones is the model of Smagorinsky [32] that is used in the present study. The Smagorinsky sgs model was initially proposed in 1963 by Joseph Smagorinsky (1963) and used in the first time in the LES simulation by Deardorff [33]. Equations for this model, which are defined by means of eddy viscosity concept, are as follow;

$$\tau_{ij}-\frac{1}{3}\delta_{ij}\tau_{kk}=-2\upsilon_{sgs}\overline{s}_{ij} \tag{10}$$

$$\upsilon_{sgs}=(C_s\Delta)^2\sqrt{2\overline{s}_{ij}\overline{s}_{ij}}\equiv(C_s\Delta)^2\left|\overline{s}\right| \tag{11}$$

$$\overline{s}_{ij}=\frac{1}{2}\left(\frac{\partial\overline{u}_i}{\partial x_j}+\frac{\partial\overline{u}_j}{\partial x_i}\right) \tag{12}$$

Here, C_S is the model constant, which in the classic Smagorinsky sgs model is constant and it does not change with time and space.

In the present study, in order to discrete the convection terms in equation (8), the QUICK scheme is applied. On the other hand, for pressure-velocity coupling, the SIMPLE algorithm [34] is applied. The dimensionless physical time steps are set to $\Delta t=0.008\ D/U_\infty$, $\Delta t=0.06\ D/U_\infty$, and $\Delta t=0.08\ D/U_\infty$ at $Re=10^3$, 10^4, and 10^5, respectively. It was found that decreasing of physical time step in each simulation did not alter results. Moreover, each time step was consisted of 20 time iterations and computing was performed with 3000, 2600, and 6000 time steps for $Re=10^3$, 10^4, and 10^5, respectively. In addition, the convergence of the numerical 3-D velocity components is established at each time step by controlling the residuals of all equations, which are defined to be solved by setting their variations less than 10^{-8}.

Grid size independence

In order to study the grid size independence of results, different grid sizes are constructed and examined for each cavity shape at each Reynolds number, distinctly. The solution was ensured to be independent from the grid quality and cell size by performing a grid size independent study on different grid sizes and control volume numbers. The details of two last grids, which all of them were hexahedral structures, are given in table 1(a) that entitled by case 1 and case 2. The grid independence study reveals rather slight differences between the case 1 and case 2 for the value of y^+ as indicated in table 1(b)-(d). However, all results of this study are reported with respect to the case 2. Moreover, for validation of results, the obtained results in this study were compared with previous experimental results and numerical predictions.

Table 3. Grid size independence study (a) number of control volumes of case 1 and case 2, (b) maximum y^+ at $Re=10^3$, (c) maximum y^+ at $Re=10^4$, (d) maximum y^+ at $Re=10^5$ between case 1 and case 2

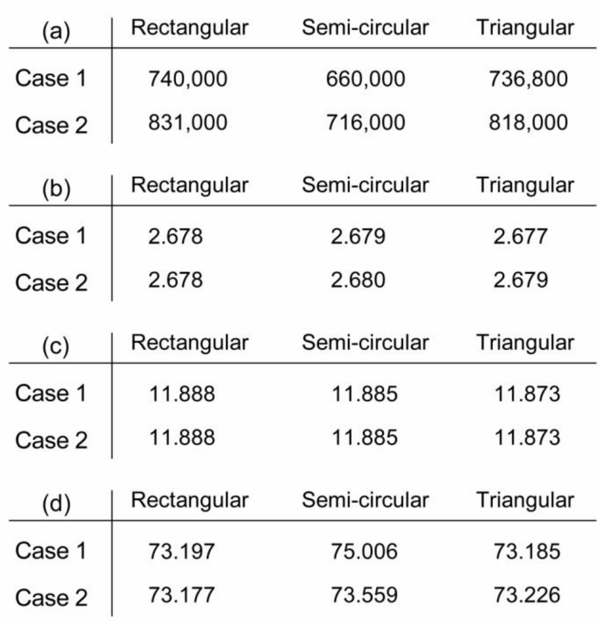

(a)	Rectangular	Semi-circular	Triangular
Case 1	740,000	660,000	736,800
Case 2	831,000	716,000	818,000

(b)	Rectangular	Semi-circular	Triangular
Case 1	2.678	2.679	2.677
Case 2	2.678	2.680	2.679

(c)	Rectangular	Semi-circular	Triangular
Case 1	11.888	11.885	11.873
Case 2	11.888	11.885	11.873

(d)	Rectangular	Semi-circular	Triangular
Case 1	73.197	75.006	73.185
Case 2	73.177	73.559	73.226

RESULTS AND DISCUSSIONS

Time-averaged flow data

In this sub-section, time-averaged flow patterns are presented. Figure 3(i) illustrates patterns of time-averaged streamlines, $\langle\psi\rangle$, within three different cavities such as rectangular, semi-circular, and triangular shapes at $Re=10^3$, 10^4, and 10^5. It is seen clearly that for the rectangular cavity at $Re=10^3$ three different vortices are developed. That is, a well-defined large-scale core vortex, V_1 which rotate clockwise and occupied the whole upper side of the cavity. In addition, a developing vortex, V_2, which rotate counter clockwise and located at the conjunction of upstream wall and lower wall of the cavity, is also evident. Finally, a small-scale corner vortex, V_3, which is located at the conjunction of downstream wall and lower wall of the cavity, is observed. As the Reynolds number increases to a value of 10^4, within the rectangular cavity, developing and corner vortices, V_2 and V_3, become smaller while the large scale core vortex, V_1, dominates whole space of cavities. Finally, as seen, at Re=10^5, developing and corner vortices, V_2 and V_3, are vanished and the large-scale vortex, V_1, occupies whole rectangular space. In the semi-circular cavity, at Re=10^3, partially similar wake structures in the rectangular cavity are developed, but the corner vortex did not appear. A noticeable event about the semi-circular cavity is the elimination of developing vortex, V_2, at Re=10^4 which reveals that the semi-circular cavity is sensitive to the increment of Reynolds number compared with other shapes in the case of lower Reynolds number. At Re=10^5, no significant changes are realized for semi-circular cavity. Responses of the triangular cavity against the Reynolds number are completely gradual and systematic comparing to the rectangular and semi-circular cavities. In other words, at Re=10^3, a large-scale core vortex, V_1, and a developing vortex, V_2, appear within the triangular cavity. Once the Reynolds number increases, the size of developing vortex, V_2, gradually decreases as indicated in the right column of Figure 3. The obtained results for vortex mechanism within all three different cavities were compared with experimental data reported by Ozalp et al. [18] as illustrated in Figure 3(ii). It is known that, in experimental works reported by Ozalp et al. [18], close to the Plexiglas surface there is a reflection laser light which deteriorates experimental readings in close region of the cavity walls.

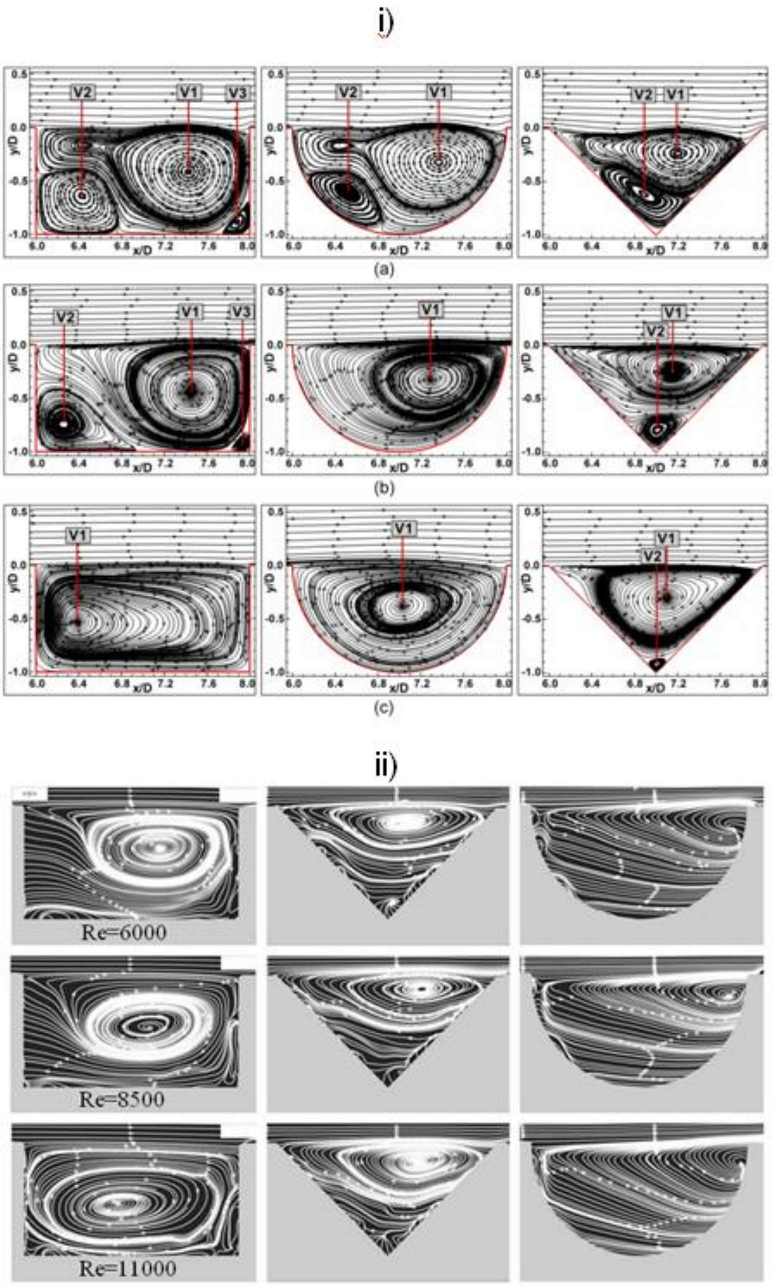

Figure 4. Time-averaged streamlines, <ψ>, patterns within three different cavities such as rectangular, semi-circular, and triangular cavities at (a) Re=10^3, (b) Re=10^4, (c)Re=10^5 (upper figure: present study and lower figure: experimental data reported by Ozalp et al., 2010)

Figure 4 shows the variation of time-averaged streamwise velocity, <u/U_∞>, which is scaled by free-stream velocity, U_∞, along the arbitrary cross sectional line at S/L=0.2 within three different cavities such as rectangular, semi-circular, and triangular shapes at Re=10^3, 10^4, and10^5. Here, "S" is measured from the upstream tip of cavities towards the downstream side and "L" is the cavity length as illustrated in right hand side images of Figure 4. At Re=10^3, flow at S/L=0.2 experiences positive values of the streamwise velocity in the lower side and negative values at upper side for the rectangular and semi-circular cavities. At Re=10^4, the flow behavior does not change significantly for the rectangular cavity, but the velocity gradient decreases for the semi-circular cavity indicating again that semi-circular cavity is more sensitive to the Reynolds number between 10^3 and 10^4 than the rectangular cavity as stated before in Figure 3. Examination of time-averaged streamwise velocity, $<u/U_\infty>$, profile for S/L=0.2 at Re=10^5 reveals that at the upstream portion of the rectangular and semi-circular cavities negative streamwise velocity values dominate at the lower sides of cavities while positive values occur on upper sides of the cavities. This flow behavior states the existing of a clockwise recirculation pattern of flow within the rectangular and semi-circular cavities at higher Reynolds numbers. In addition, at S/L=0.2, Flow structures in the triangular cavity do not alter significantly by increasing the Reynolds number due to the very small streamwise velocity gradients as indicated in the last image of Figure 4.

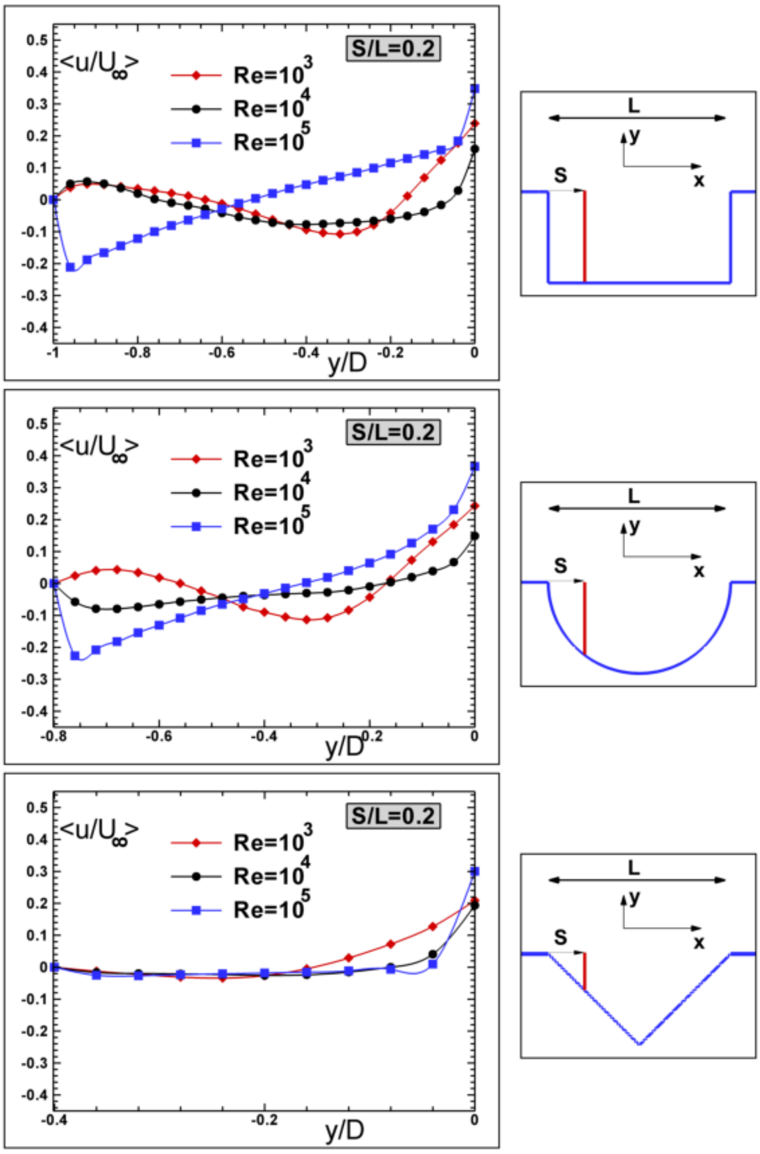

Figure 5. Time-averaged streamwise velocity, $<u/U_\infty>$, distributions within the three different cavities such as rectangular, semi-circular, and triangular cavities along S/L=0.2 in which "S" is measured from the tip of cavity towards the downstream side and "L" is the cavity length at (a) Re=10^3, (b) Re=10^4, (c) Re=10^5

Variation of time-averaged streamwise velocity, <u/U∞>, illustrated in Figure 5 along the cross sectional lines at the location of S/L=0.5 within three different cavities. Examination of first image reveals that, at S/L=0.5, within the rectangular and semi-circular cavities the negative streamwise velocity values dominate at the regions close to lower wall of cavities while the positive streamwise velocity values are mostly developed at higher elevations. In addition, once the Reynolds number increases, the velocity gradient increases within cavities. For S/L=0.5, flow in the triangular cavity experiences positive streamwise velocity values at lower elevations in the cases of Re=10^3 and 10^4. On the other hand, at Re=10^5, the negative streamwise velocity values are developed at the lower elevations in the triangular cavity along S/L=0.5 as demonstrated in the last image of Figure 5.

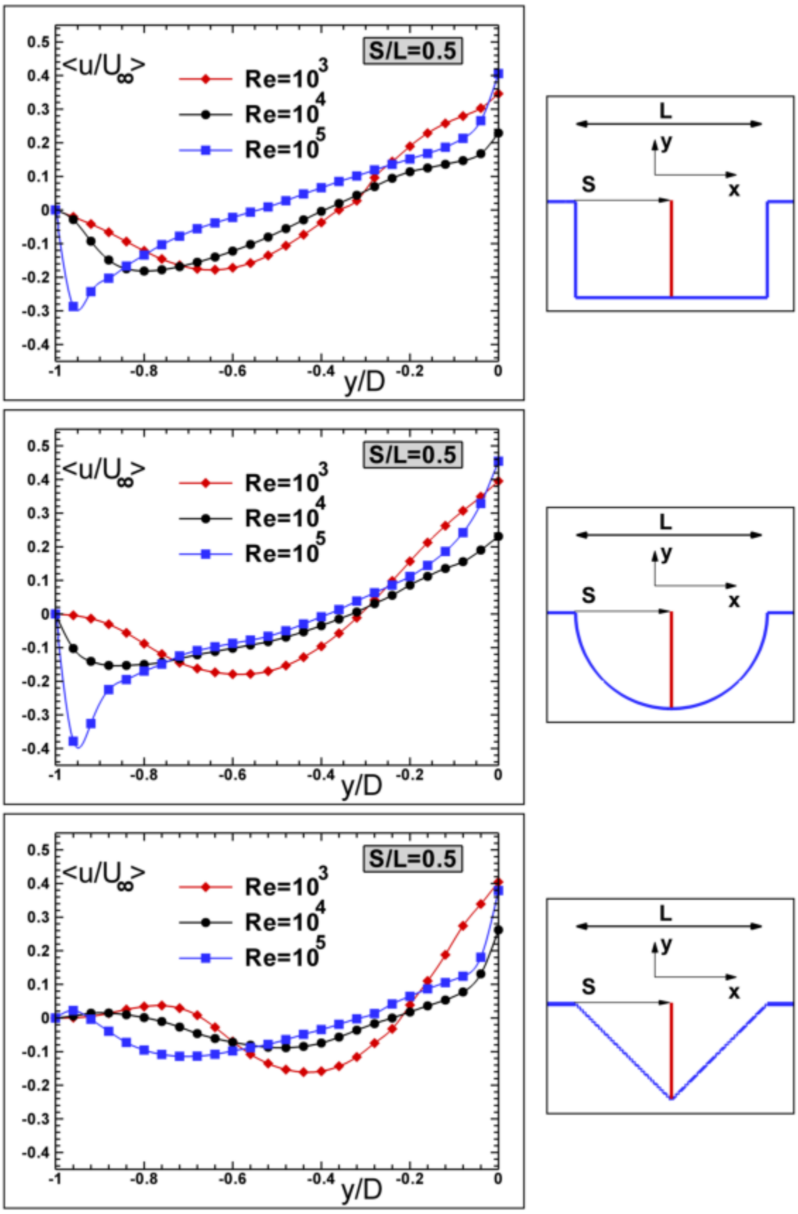

Figure 6. Time-averaged streamwise velocity, <u/U∞>, distributions within the three different cavities such as rectangular, semi-circular, and triangular cavities along S/L=0.5 in which "S" is measured from the tip of cavity towards the downstream side and "L" is the cavity length at (a) Re=103, (b) Re=104, (c) Re=105

Figure 6 illustrates the variation of time-averaged streamwise velocity component, $<u/U_\infty>$, along S/L=0.8 within all cases of cavities. Despite of the fact that, at S/L=0.8, the negative streamwise velocity values are dominated at lower elevations of three different cavity shapes for all Reynolds numbers however, flow structure within the triangular cavity did not alter significantly by increasing the Reynolds number as previously stated in Figure 3.

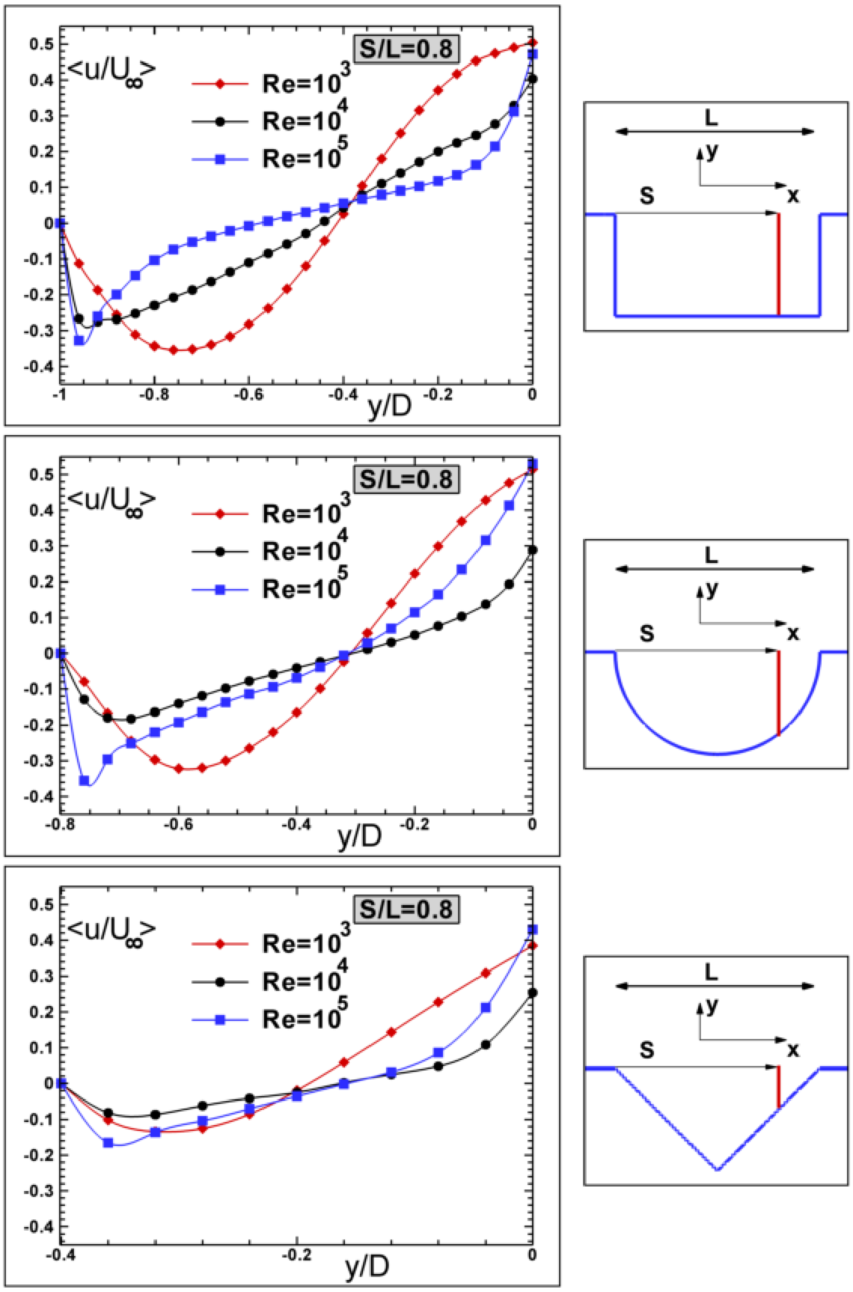

Figure 7. Time-averaged streamwise velocity, <u/U∞>, distributions within the three different cavities such as rectangular, semi-circular, and triangular cavities along S/L=0.8 in which "S" is measured from the tip of cavity towards the downstream side and "L" is the cavity length at (a) Re=103, (b) Re=104, (c) Re=105

Figure 7 shows time-averaged static pressure,$<P_s/0.5\rho U^2_\infty>$, patterns which are scaled by dynamic pressure for all cases of cavities at $Re=10^3$, 10^4, and10^5. Examination of time-averaged static pressure, $<P_s/0.5\rho U^2_\infty>$, at $Re=10^3$ reveals that a maximum negative pressure pocket is developed near the downstream side of all cavities. The value of time-averaged static pressure, $\langle P_s/0.5\rho U^2_\infty \rangle$, for the triangular cavity is smaller compared with other cases. An increase of the Reynolds number, causes an extension on the negative pressure pocket within cavities at Re=10^4. Finally, the negative static pressure is observed in the entire volume of the cavities. Comparison of images in Figure 7 indicates an unexpected pressure jump in the semi-circular cavity at Re=10^5. This flow behavior of the semi-circular cavity states that the rates of momentum transfer and kinetic energy decrease in the higher Reynolds number. A systematic increase in momentum transfer with increasing of the Reynolds number is seen in the rectangular cavity as illustrated in Figure 7. Further examination of Figure 7 states that the triangular cavity imposes a smaller drag on the fluid flow in comparison to the rectangular and semi-circular cavities at all Reynolds numbers.

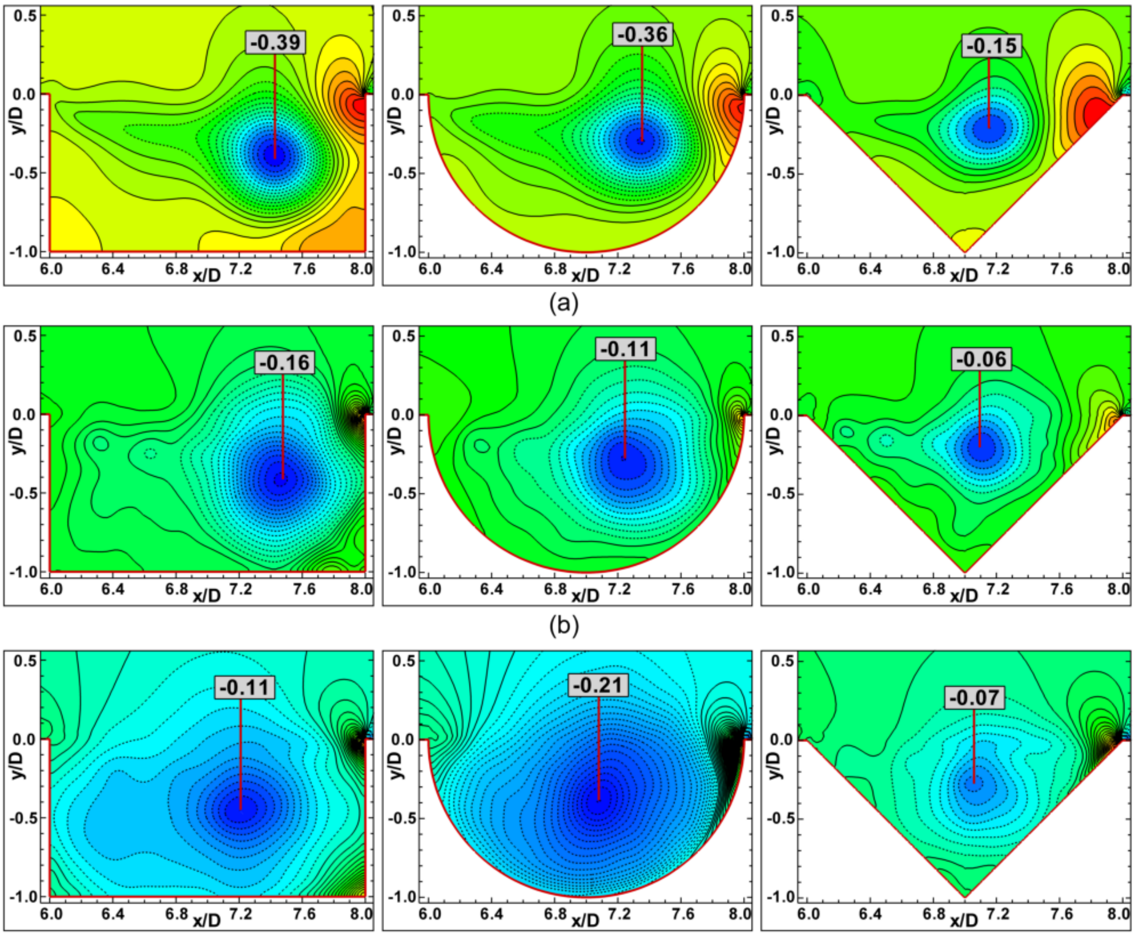

(a)

(b)

(c)

Figure 8. Time-averaged static pressure, $\langle P_s/0.5\rho U^2_\infty \rangle$, patterns within three different cavities such as rectangular, semi-circular, and triangular cavities at (a) Re=10^3(contour increment: 0.0275), (b) Re=10^4 (contour increment: 0.01), (c) Re=10^5(contour increment: 0.01)

Patterns of root mean square of fluctuating pressure, $\langle P_{rms}/0.5\rho U^2_\infty \rangle$, for all cavities at Re=10^3, 10^4, and10^5 are illustrated in Figure 8, which is made dimensionless by dynamic pressure. For each cavity, at Re=10^3, a peak value is detected near the downstream wall. An interesting result is obtained as the Reynolds number increases. In other words, increasing the Reynolds number decreases the value of $<P_{rms}/0.5\rho U^2_\infty>$, within cavities revealing an increase on the turbulent kinetic energy. The minimum value of $<P_{rms}/0.5\rho U^2_\infty>$, which corresponds to the maximum turbulent kinetic energy are obtained within cavities once the Reynolds number reaches a value of 10^5. The root mean square of fluctuating pressure, $<P_{rms}/0.5\rho U^2_\infty>$, at $Re=10^5$ is higher within the semi-circular cavity case which corresponds to the lower turbulence intensity and turbulent kinetic energy compared with rectangular and triangular cavities.

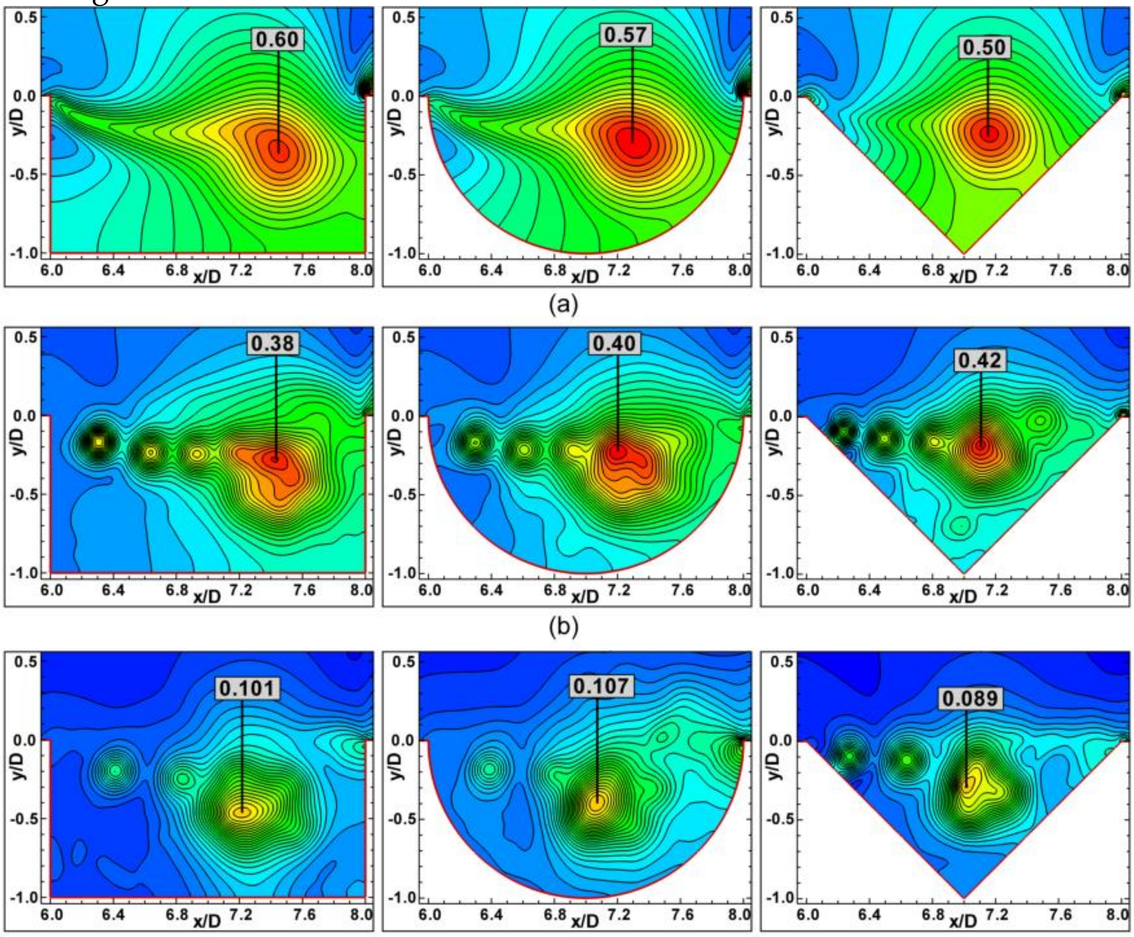

(a)

(b)

(c)

Figure 9. Time-averaged root mean square of fluctuating pressure, $<P_{rms}/0.5\rho U^2_\infty>$,patterns within three different cavities such as rectangular, semi-circular, and triangular cavities at (a) $Re=10^3$(contour increment: 0.025), (b) $Re=10^4$ (contour increment: 0.015), (c) $Re=10^5$(contour increment: 0.015)

Instantaneous flow data

It is known that the instantaneous flow data are useful and necessary for analysis of unsteady flows such as understanding of the physics of flow and statistical studies of turbulence in detail. Figure 9 illustrates patterns of the instantaneous streamlines, ψ, within all cases of cavities at $Re=10^3$, 10^4, and 10^5. Images of Figure 9 give useful information on the wake deformation with respect to the cavity shape and the Reynolds number. At $Re=10^3$, a systematic wake deformation is recognized for all cases of cavities in this study. The size of the large-scale core vortex, V_1, becomes smaller gradually within the period of time while the developing vortex, V_2, shows a limited expansion within all three cavities. It is due to this fact that flow within cavities at $Re=10^3$, except at the separation points, is laminar. Having Reynolds number as $Re=10^4$, a wake deformation is seen within all cavities. The location of large-scale vortex changes within the cavities indicating occurrence of the higher flow recirculation within cavities while the large-scale and developing vortices, V_1 and V_2, keep their primary shapes more or less same. A noticeable and important results are obtained at $Re=10^5$. That is seen clearly in the last row of Figure 9, at $Re=10^5$, wake deformation becomes stronger in the rectangular and triangular cavities while within the semi-circular cavity, a large scale core vortex, V_1, shows a tendency to keep its primary shape more or less same. On the other hand, the small-scale vortices appear within the rectangular and triangular cavities which indicates the higher rate of turbulence at $Re=10^5$ within the rectangular and triangular cavities. In addition, the lower turbulence intensity in the semi-circular cavity is detected at high Reynolds numbers compared with other cases.

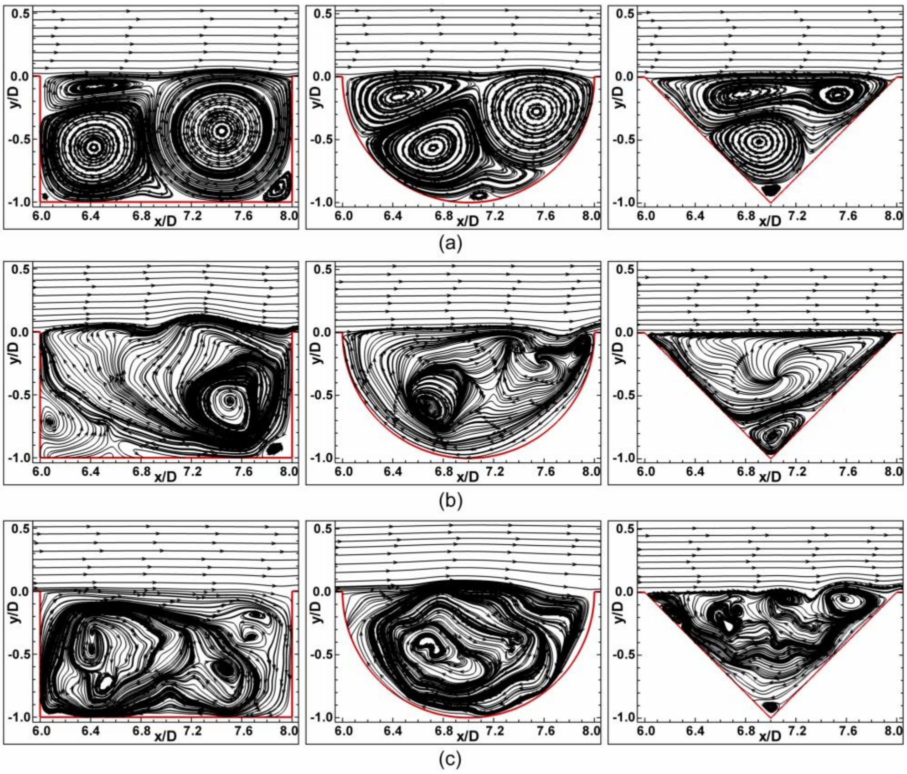

(a)

(b)

(c)

Figure 10. Instantaneous streamlines, ψ, patterns within three different cavities such as rectangular, semi-circular, and triangular cavities at (a) Re=103, (b) Re=104, (c) Re=105

Wakes deformation within different cavities at various Reynolds numbers are understood well by examination of vortical structures. Figure 10 demonstrates patterns of normalized vortical structure, $\omega_z D/U_\infty$, within the rectangular, semi-circular, and triangular cavities at $Re=10^3$, 10^4, and 10^5. It is seen clearly that at $Re=10^3$, the large-scale vortical structures are detected in all cases of cavities. By appearance of small scale eddies, at $Re=10^4$, flow entrainment increases and hence kinetic energy of flow within the cavities increases as seen in Figure 10. Increasing the kinetic energy within the cavity develops a flow recirculation region near the cavity wall for all cases of cavities. This flow recirculation is more evident in the rectangular cavity than two other cases indicating the higher turbulence intensity. By increasing the Reynolds number up to Re=10^5, the appearance of small scale eddies becomes highly detectable. Furthermore, the turbulence intensity and the rate of flow entrainment within cavities increase. Finally, small scale eddies within cavities at higher Reynolds numbers increases the interaction between eddies. As a result, it is expected to increase the eddy viscosity as the Reynolds number increases.

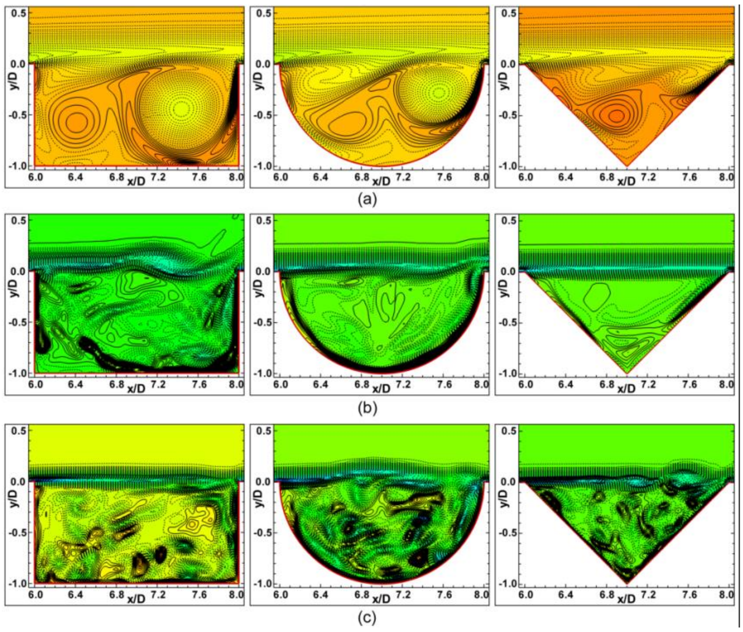

Figure 11. Instantaneous vortical structure, ωzD/U∞, patterns within three different cavities such as rectangular, semi-circular, and triangular cavities at (a) Re=103, (b) Re=104, (c) Re=105

Since the turbulent flow has a three-dimensional nature, one need to interpret the vortical flow structure in vertical direction, namely in the y-z plane. Figure 11 illustrates the numerical prediction of normalized instantaneous vortical structure $\omega_y D/U_\infty$ in y-z plane located at the centre of all cases of cavities. First and second rows of Figure 11 shows the patterns of $\omega_y D/U_\infty$ at Re=10^{4}and 10^5, respectively. Like as the previous figures, dashed lines indicate the negative values of vortical structures. The flow seems to have a coherent turbulent structure at Re=10^4 within the cavities. Increasing the Reynolds number up to 10^5 causes the large vortical structures to be broken into smaller structures as seen in the second row of Figure 11. As a result, flow entrainment and the rate of eddy viscosity will increase within the cavities at higher Reynolds numbers.

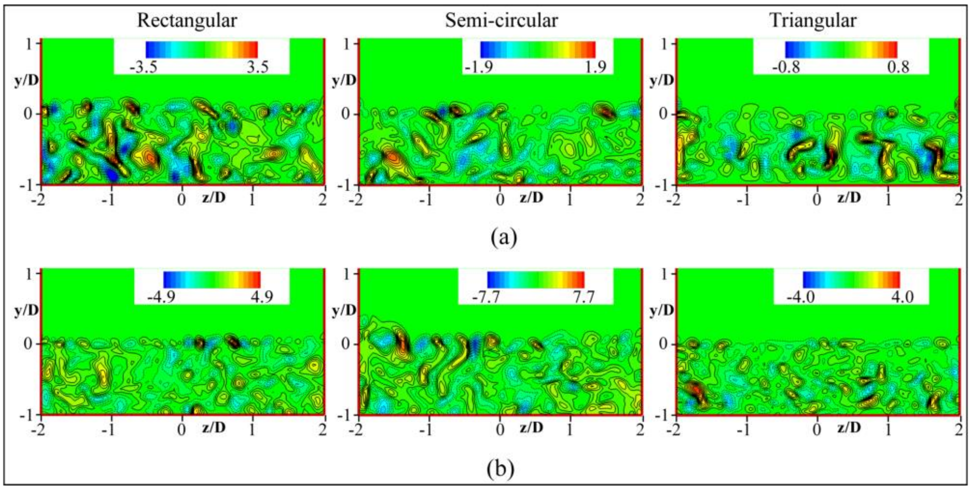

Figure 12. Instantaneous vortical structure, ωyD/U∞, patterns within three different cavities such as rectangular, semi-circular, and triangular cavities at (a) Re=104, (b) Re=105

Figure 12 demonstrates the iso-surface of vortical flow structures in all cases of cavities at $Re=10^3$, 10^4, and 10^5. In general, for all cavities the flow structure is unchanged in spanwise direction and flow can be assumed to be laminar within cavities at $R=10^3$. On the other hand, chaotic structures within cavities are developed and flow become three-dimensional when the Reynolds number increases to a value of $Re=10^4$. Increasing the Reynolds number to a value of 10^5, causes the larger scale eddies break into the smaller eddies resulting in the higher turbulence intensity, the higher eddy viscosity, and the higher flow entrainment within all cavities.

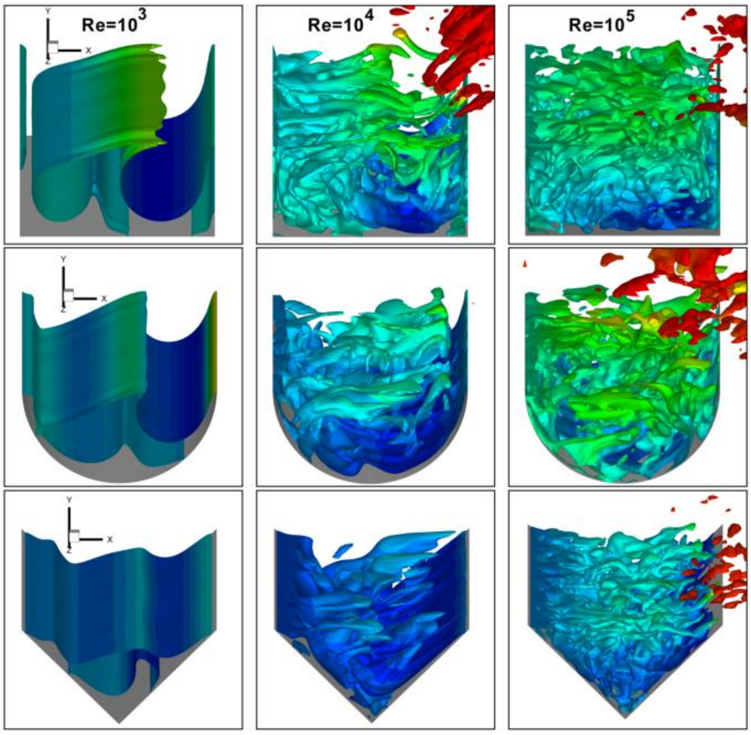

Figure 13. Instantaneous vortical structure iso-surfaces within three different cavities such as rectangular, semi-circular, and triangular cavities at (a) Re=103, (b) Re=104, (c) Re=105

CONCLUSION

Flow structures within the rectangular, semi-circular, and triangular cavities at Re=10^3, 10^4, and 10^5 is studied numerically using Large Eddy Simulation. It is observed that flow within the cavities alters as a function of the shape and the Reynolds number. At Re=10^3, flow within the cavities, except at separation points, is laminar and two-dimensional without changes of flow characteristics in the spanwise direction. In other words, at Re=10^3, some different vortical flow structures are detected within cavities in the flow direction, for example, the large scale core vortex, V_1, developing vortex, V_2, and corner vortex, V_3, within the rectangular cavity and the large scale core vortex, V_1, developing vortex, V_2, within the semi-circular and triangular cavities are developed. Once the Reynolds number increases to a value of 10^4, the semi-circular cavity affected substantially comparing to other cavities. For the high Reynolds number, Re=10^5, values of time-average static pressure and fluctuating static pressure are higher within the semi-circular cavity. In contrast, the momentum transfer and the turbulent kinetic energy are lower in comparison to the rectangular and triangular cavities.

Examination of instantaneous flow data stated that by increasing the Reynolds number the large scale eddies break into small scale eddies within all cases of cavities and flow becomes turbulent, completely. This situation increases the flow entrainment and eddy viscosity in cavities. In the continuations of the present work, namely as a future work, the following recommendations can be made. For example, investigation on the effects of cavity aspect ratio, as an effective parameter on the flow structure, on the heat and fluid flow behavior with various cavity shapes may be useful for heat exchanger applications with various types. Alternatively, applications of cavities with different shapes at very large Reynolds number, namely supersonic flow, can be recommended since they can be interested in aerodynamic applications.

ACKNOWLEDGMENTS

The authors would like to acknowledge the funding of the Research Projects Office of Cukurova University under contract No: MMF 2012D17.

REFERENCES

Chaing, T. P., Hwang, R. R., & Sheu, W. H. (1996). Finite volume analysis of spiral motion in a rectangular lid-driven cavity. International journal for numerical methods in fluids, 23(4), 325-346.

Chiang, T. P., Sheu, W. H., & Hwang, R. R. (1998). Effect of Reynolds number on the eddy structure in a lid-driven cavity. International journal for numerical methods in fluids, 26(5), 557-579.

Chiang, T. P., & Sheu, W. H. (1997). Numerical prediction of eddy structure in a shear-driven cavity. Computational Mechanics, 20(4), 379-396.

Albensoeder, S., Kuhlmann, H. C., & Rath, H. J. (2001). Multiplicity of steady two-dimensional flows in two-sided lid-driven cavities. Theoretical and Computational Fluid Dynamics, 14(4), 223-241.

Khanafer, K., & Vafai, K. (2002). Double-diffusive mixed convection in a lid-driven enclosure filled with a fluid-saturated porous medium. Numerical Heat Transfer: Part A: Applications, 42(5), 465-486.

Chen, C. L., & Cheng, C. H. (2004). Experimental and numerical study of mixed convection and flow pattern in a lid-driven arc-shape cavity. Heat and mass transfer, 41(1), 58-66.

Sun, K. H., Pyle, D. L., Baines, M. J., Hall-Taylor, N., & Fitt, A. D. (2006). Velocity profiles and frictional pressure drop for shear thinning materials in lid-driven cavities with fully developed axial flow. Chemical engineering science,61(14), 4697-4706.

Sørensen, J. N., Naumov, I., & Mikkelsen, R. (2006). Experimental investigation of three-dimensional flow instabilities in a rotating lid-driven cavity. Experiments in fluids, 41(3), 425-440.

Bouffanais, R., Deville, M. O., Fischer, P. F., Leriche, E., & Weill, D. (2006). Large-eddy simulation of the lid-driven cubic cavity flow by the spectral element method. Journal of Scientific Computing, 27(1), 151-162.

Noor, D. Z., Kanna, P. R., & Chern, M. J. (2009). Flow and heat transfer in a driven square cavity with double-sided oscillating lids in anti-phase.International Journal of Heat and Mass Transfer, 52(13), 3009-3023.

Mercan, H., & Atalık, K. (2009). Vortex formation in lid-driven arc-shape cavity flows at high Reynolds numbers. European Journal of Mechanics-B/Fluids,28(1), 61-71.

Oueslati, F., Beya, B. B., & Lili, T. (2011). Aspect ratio effects on three-dimensional incompressible flow in a two-sided non-facing lid-driven parallelepiped cavity. Comptes Rendus Mecanique, 339(10), 655-665.

Haque, S., Lashgari, I., Giannetti, F., & Brandt, L. (2012). Stability of fluids with shear-dependent viscosity in the lid-driven cavity. Journal of Non-Newtonian Fluid Mechanics, 173, 49-61.

Manca, O., Nardini, S., & Vafai, K. (2006). Experimental investigation of mixed convection in a channel with an open cavity. Experimental heat transfer, 19(1), 53-68.

Rauwoens, P., Vierendeels, J., & Merci, B. (2008). Numerical study of the flow in a three-dimensional thermally driven cavity. Journal of Computational and Applied Mathematics, 215(2), 538-546.

John, B., Gu, X. J., & Emerson, D. R. (2010). Investigation of heat and mass transfer in a lid-driven cavity under nonequilibrium flow conditions. Numerical Heat Transfer, Part B: Fundamentals, 58(5), 287-303.

Dos Santos, E. D., Piccoli, G. L., França, F. H. R., & Petry, A. P. (2011). Analysis of mixed convection in transient laminar and turbulent flows in driven cavities. International Journal of Heat and Mass Transfer, 54(21), 4585-4595.

Ozalp, C., Pinarbasi, A., & Sahin, B. (2010). Experimental measurement of flow past cavities of different shapes. Experimental Thermal and Fluid Science,34(5), 505-515.

Saqr, K. M., Aly, H. S., Kassem, H. I., Sies, M. M., & Wahid, M. A. (2010). Computations of shear driven vortex flow in a cylindrical cavity using a modified k-ε turbulence model. International Communications in Heat and Mass Transfer, 37(8), 1072-1077.

Saqr, K. M., Aly, H. S., Kassem, H. I., Sies, M. M., & Wahid, M. A. (2010, July). Large Eddy Simulation of shear-driven vortex flow in a cylindrical cavity. In Proceedings of the 2010 international conference on theoretical and applied mechanics, and 2010 international conference on Fluid mechanics and heat & mass transfer (pp. 84-87). World Scientific and Engineering Academy and Society (WSEAS).

Ryu, Y. H., & Baik, J. J. (2009). Flow and dispersion in an urban cubical cavity.Atmospheric Environment, 43(10), 1721-1729.

Zhang, T., Shi, B., & Chai, Z. (2010). Lattice Boltzmann simulation of lid-driven flow in trapezoidal cavities. Computers & Fluids, 39(10), 1977-1989.

Peng, S. H., & Davidson, L. (2001). Large eddy simulation for turbulent buoyant flow in a confined cavity. International Journal of Heat and Fluid Flow, 22(3), 323-331.

Perumal, D. A., & Dass, A. K. (2011). Multiplicity of steady solutions in two-dimensional lid-driven cavity flows by Lattice Boltzmann Method. Computers & Mathematics with Applications, 61(12), 3711-3721.

Chen, S., Liu, H., & Zheng, C. (2012). Numerical study of turbulent double-diffusive natural convection in a square cavity by LES-based lattice Boltzmann model. International Journal of Heat and Mass Transfer, 55(17), 4862-4870.

Lawson, S. J., & Barakos, G. N. (2011). Review of numerical simulations for high-speed, turbulent cavity flows. Progress in Aerospace Sciences, 47(3), 186-216.

Lawson, S. J., & Barakos, G. N. (2011). Review of numerical simulations for high-speed, turbulent cavity flows. Progress in Aerospace Sciences, 47(3), 186-216.

Salinas-Vazquez, M., Vicente, W., Martinez, E., & Barrios, E. (2011). Large eddy simulation of a confined square cavity with natural convection based on compressible flow equations. International Journal of Heat and Fluid Flow,32(5), 876-888.

Goncalvès, E., & Decaix, J. (2012). Wall model and mesh influence study for partial cavities. European Journal of Mechanics-B/Fluids, 31, 12-29.

Hassanzadeh, R., Sahin, B., & Ozgoren, M. (2011). Numerical investigation of flow structures around a sphere. International Journal of Computational Fluid Dynamics, 25(10), 535-545. Krajnović, S., Ringqvist, P., Nakade, K., & Basara, B. (2012). Large eddy simulation of the flow around a simplified train moving through a crosswind flow. Journal of Wind Engineering and Industrial Aerodynamics, 110, 86-99.

Smagorinsky, J. (1963). General circulation experiments with the primitive equations: I. the basic experiment*. Monthly weather review, 91(3), 99-164.

Deardorff, J. W. (1973). The use of subgrid transport equations in a three-dimensional model of atmospheric turbulence. Journal of Fluids Engineering,95(3), 429-438.

Patankar, S. (1980). Numerical heat transfer and fluid flow. CRC press.